Influence Of Time Step On Accuracy And Convergence In Fluid–Structure Interaction Analysis

Xuan-Thuc Nguyen[1], Ngoc-Quynh Nguyen[1], Le-Minh Nguyen[1], Thi-Tuyet-Nhung Le[2], Dai-Cuong Pham[2], and Dinh-Quy Vu[2*]

[1] *Viettel High Technology Industries Corporation – Viettel Group, Hanoi, Vietnam*
[2] *School of Mechanical Engineering, Hanoi University of Science and Technology, Hanoi, Vietnam*
[*] *Corresponding author. E-mail: quy.vudinh@hust.edu.vn*

Received: March 07, 2026; Accepted: July 11, 2026

Fluid–Structure Interaction (FSI) is a multidisciplinary research field that has drawn significant attention across various domains, including aerospace, biomedical engineering, agriculture, industry, and renewable energy. The finite element method (FEM) has become a leading computational tool for investigating these coupled phenomena, enabling more accurate prediction of the interactions between fluids and solids. Although numerical FSI simulations are more economical than physical experiments, they require substantial computational resources. This study focuses on the influence of time step size on the accuracy and convergence of coupled FSI simulations. A cantilever beam model is adopted as the benchmark case and analyzed using the ANSYS software suite. The time step of the fluid solver and the sub-step size of the structural solver are systematically varied to determine the optimal configuration that ensures accuracy while minimizing computation time. The amplitude and frequency responses obtained from the coupled solver are validated against reference results from published literature. The optimized time step and sub-step selection strategy is then applied to more complex FSI simulations, including a cropped delta wing and a lightweight composite UAV wing, to evaluate flutter behavior within their operating envelopes.

Keywords: Computational Fluid Dynamics (CFD); Fluid–Structure Interaction (FSI); Time Step, Sub-Step; Convergence

http://dx.doi.org/10.6180/jase.202611_34.009

1. Introduction

Fluid–Structure Interaction (FSI) is widely applied across engineering fields to model the coupled behavior between fluids and deformable structures. In biomedical engineering, FSI is used to study cardiovascular mechanisms such as aneurysm development, valve dynamics, and blood–vessel interaction. Notable works include FSI simulations of venous valves by Wang et al. [1] and Marcinnò et al. [2]. Furthermore, whole-heart and valve-specific studies were conducted by Tango et al. [3], Feng et al. [4], Abdi et al. [5], and Cai et al. [6]. Additionally, Souche and Valen-Sendstad [7] investigated turbulent-like aneurysm flows. These studies highlight FSI's importance in predicting physiological behavior, assessing risks, and supporting medical-device and artificial-valve design. In agriculture, FSI has been used to analyze UAV downwash effects on plant canopies, as demonstrated by Mai et al. [8] and Cui et al. [9]. In industrial and marine engineering, CFD and FSI applications include the study of offshore structures by Liao et al. [10] and submerged vegetation deformation by Prüter et al. [11]. Additionally, these simulations have been applied by Sakran et al. [12] to optimize pump blade angles, by Darbhamulla and Jaiman [13] to mitigate rotor cavitation, and by Firdaus et al. [14] to analyze seaplane water impacts. Other research focuses on wind-turbine blade fatigue and deformation by Shakya et al. [15] and Yuan et al. [16], along with flow-guiding optimization in corrosive pipelines by Cui et al. [17]. In aeronautics, FSI has become essential for aeroelastic analysis. Key studies include staggered CFD–CSM coupling for wing vibration prediction by Mihaila-Andres et al. [18] and vortex-induced vibration modeling by Di Domenico et al. [19]. Other research has focused on flutter-speed enhancement through composite optimization by Torregrosa et al. [20] and analysis of flow-induced vibrations on a NACA 0015 hydrofoil by Salmon and Chatellier [21]. Recently, significant research has also addressed morphing-wing aerodynamic stability [22–25].

Despite its broad application, the accuracy and stability of FSI simulations heavily depend on several major factors. Recent studies highlight the significant impact of spatial discretization at the fluid-solid interface [26, 27] and the mathematical stability of chosen coupling strategies [28]. Beyond these, temporal discretization remains a paramount factor. While advanced time-adaptive methods have been proposed [29], systematically optimizing the combination of the global fluid time step and structural sub-step in standard partitioned solvers remains critical. Therefore, this study focuses on the influence of time step size on the accuracy and convergence of coupled FSI simulations.

This project adopts theoretical foundations from ANSYS Help documentation and Introduction to Aircraft Aeroelasticity and Whirl Flutter [30]. Benchmark cases from Slone et al. [31], Peng and Han [32], and Kumar et al. [33] are used to validate the numerical approach. The study performs FSI simulations on a cantilever beam and a cropped delta wing as preliminary validation steps, followed by a full FSI analysis of a lightweight composite UAV wing.

2. Theory and formula

The FSI analysis in this study adopts a partitioned time-domain approach, in which the CFD and CSD solvers are treated separately. The governing equations and numerical solution procedures for each solver are discussed in the following sections.

2.1. Governing Equations for Fluid Flow (CFD)

The Finite Volume Method (FVM) is used to discretize the Reynolds-averaged Navier–Stokes (RANS) equations for unsteady compressible flow with the $\mathrm{k}-\omega$ SST turbulence model. These equations, based on the conservation of mass, momentum, and energy, describe the motion of compressible fluids with variable density. In conservative tensor notation, assuming time-averaged quantities for the mean flow, the governing equations are expressed as follows:

The continuity equation ensures the conservation of mass:

$$\frac{\partial \rho}{\partial t} + \frac{\partial (\rho u_i)}{\partial x_i} = 0 \tag{1}$$

The conservation of momentum equation, incorporating the effects of turbulence, is given by:

$$\frac{\partial (\rho u_i)}{\partial t} + \frac{\partial \left(\rho u_i u_j\right)}{\partial x_j} = -\frac{\partial p}{\partial x_i} + \frac{\partial}{\partial x_j}\left(\tau_{ij} - \rho \overline{u_i' u_j'}\right) + \rho f_{b,i} \tag{2}$$

The energy equation states that the change in the total energy of the fluid must equal the amount of energy added to or removed from the system:

$$\begin{aligned} &\frac{\partial (\rho h_{tot})}{\partial t} - \frac{\partial p}{\partial t} + \frac{\partial \left(\rho u_j h_{tot}\right)}{\partial x_j} \\ &= \frac{\partial}{\partial x_j}\left(\lambda_{eff}\frac{\partial T}{\partial x_j}\right) + \frac{\partial}{\partial x_j}\left[u_i\left(\tau_{ij} - \rho\overline{u_i' u_j'}\right)\right] + S_E \end{aligned} \tag{3}$$

Where ρ is the fluid density, t is time, u_i is the mean velocity vector component, and x_i represents the Cartesian coordinates. The static pressure is denoted by p, and $f_{b,i}$ represents the body forces (typically gravity). In the momentum and energy equations, τ_{ij} is the mean viscous stress tensor for a Newtonian fluid, defined as:

$$\tau_{ij} = \mu\left(\frac{\partial u_i}{\partial x_j} + \frac{\partial u_j}{\partial x_i}\right) - \frac{2}{3}\mu\frac{\partial u_k}{\partial x_k}\delta_{ij} \tag{4}$$

Where μ is the dynamic viscosity and δ_{ij} is the Kronecker delta. The term $-\rho\overline{u'_i u'_j}$ represents the Reynolds stress tensor, accounting for momentum transfer due to turbulent fluctuations.

For the energy equation, h_{tot} denotes the total enthalpy, T is the temperature, and S_E represents external energy sources. The effective thermal conductivity is given by $\lambda_{\text{eff}} = \lambda + \lambda_t$, where λ is the molecular thermal conductivity and λ_t is the turbulent thermal conductivity. The term $\frac{\partial}{\partial x_j}\left[u_i\left(\tau_{ij} - \rho\overline{u_i' u_j'}\right)\right]$ is the viscous dissipation term, incorporating both mean and turbulent stresses.

2.2. Governing Equations for Structural Dynamics (CSD)

The structural dynamic equations describe the motion of a structure subjected to external loads and can be written in matrix form as follows:

$$[M]\{\ddot{u}\} + [C]\{\dot{u}\} + [K]\{u\} = \{F(t)\} \tag{5}$$

The elasticity equation describes the relationship between strain and stress in the structure under external loading.

$$\sigma = E.\varepsilon \tag{6}$$

In these equations, $[M]$, $[C]$, and $[K]$ are the mass, damping, and stiffness matrices, respectively, and $\{F(t)\}$ is the applied load vector representing pressure and shear forces. The vectors $\{\ddot{u}\}$, $\{\dot{u}\}$, and $\{u\}$ denote acceleration, velocity, and displacement, respectively. Since the analysis includes geometric nonlinearities, the stiffness matrix becomes a function of the nodal displacements. Here, σ represents the stress, E is the elastic (Young's) modulus, and ε denotes the strain. 2.3. Coupling Between CFD and CSD

A two-way coupling strategy is used to capture the flow-induced micro-deformation. Simulations are performed in ANSYS Workbench, where Fluent solves the fluid domain and Mechanical handles the structural domain, linked via the System Coupling module. In each coupling step, the CFD solver first converges, and the resulting aerodynamic pressures are passed to the FEA model as loads. The structural deformation and stress are then computed and mapped back to the fluid mesh. This iterative exchange continues until changes in aerodynamic forces and displacements fall below a specified tolerance. Fig. 1 illustrates the workflow.

To ensure the numerical stability and accuracy of the two-way FSI simulations, strict convergence criteria were established for the individual solvers as well as the system coupling interface. Within the fluid domain (CFD), the residual convergence targets were stringently set to 1×10^{-6} for the x, y, and z velocity components, 5×10^{-3} for the continuity equation, and 1×10^{-3} for the $k - \omega$ turbulence parameters. For the structural domain (CSD), the convergence was governed by the solver's default criteria (Program Controlled), which enforces a strict 0.5% tolerance limit on the L2-norm of the internal force imbalance during the Newton-Raphson iterations. Furthermore, to guarantee the physical equilibrium of the fluid-structure interface within each time step, the Root Mean Square (RMS) convergence target for the bidirectional data transfer was set to $0.01(1\%)$. An under-relaxation factor of 1.0 was applied to this inter-field transfer, while a maximum of 100 inner iterations per global time step was specified for the fluid solver. Furthermore, boundary deformations were accommodated using a hybrid Smoothing and Remeshing dynamic mesh strategy with the Implicit Update mechanism activated. Mesh integrity was continuously verified throughout the deformation cycles, maintaining a maximum cell skewness of 0.9 and a face skewness of 0.7 to preserve computational fidelity.

The bidirectional FSI analysis utilizes a partitioned implicit coupling approach, linking the Fluent pressure-based implicit fluid solver with the implicit Transient Structural solver in ANSYS Mechanical. The implicit time integration formulation is unconditionally stable, the selection of the global time step is governed primarily by the temporal resolution requirements of the structural vibration frequency (points per cycle) rather than the strict Courant-Friedrichs-Lewy (CFL) constraints of explicit numerical schemes.

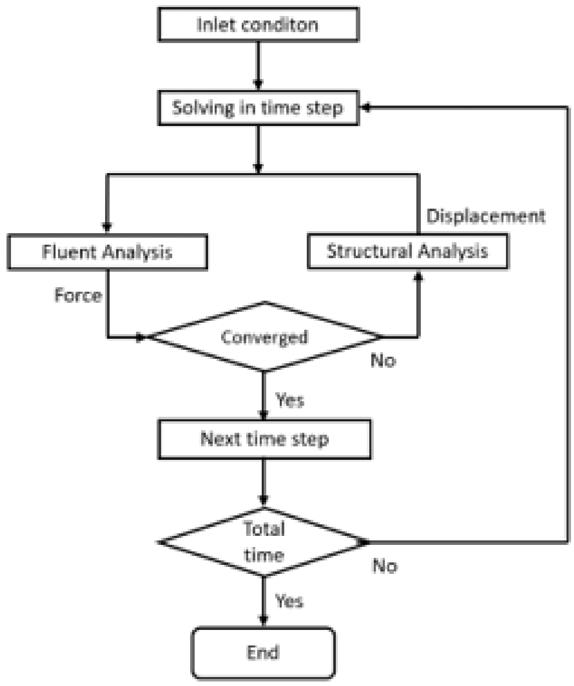

Fig. 1. Schematic of the two-way FSI process.

2.3. Model Verification

To investigate the dynamic fluid–structure interaction behavior of continuously deforming structures, a cantilever beam is selected as the verification model. The results obtained in this study are compared with those published in reference [31].

2.3.1. Model and Mesh

This model is based on the experimental model of Slone [31]. The Beam domain contains 24,705 nodes and 5,120 elements, whereas the Fluid domain includes 104,656 nodes and 95,960 elements. The aerodynamic mesh for the fluid region is illustrated in Fig. 2.

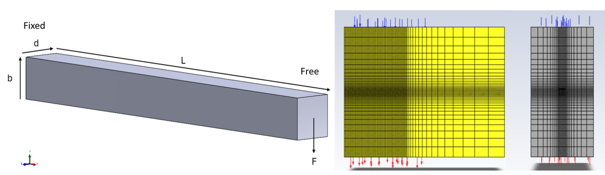

Fig. 2. Structural model and CFD model.

The density of the beam1 ρ is 2600 $\text{kg}\cdot\text{m}^{-3}$, the Young's modulus is 21.0 GPa, and the Poisson's ratio is 0.3 . A modal analysis is conducted to determine the natural frequencies of the structure, yielding a first-mode natural frequency of 2.28 Hz, which corresponds to a vibration period of 0.44 s. The required physical time increment, Δt (hereafter referred to as the time step), for the transient analysis is determined using the general relation:

$$\Delta t = \frac{1}{N \cdot f} \tag{7}$$

where N is the number of time steps per vibration cycle (points per cycle) and f is the structural natural frequency. In this study, to ensure sufficient temporal resolution for the baseline validation, N is initially chosen as 20 . A transient structural analysis is performed using the time step calculated from Eq. (7), resulting in a time step of 0.022 s. The boundary conditions of the beam consist of a clamped face at $x^-$and a free end at x^+. A concentrated load of 1.05 MN is applied at the center of the free surface.

The boundary conditions for the Fluent solver are defined as follows. The inlet velocity at the y^+face is set to 100 m/s, while the y^-face is specified as a pressure outlet with a gauge pressure of 0 Pa . Furthermore, the x^-face is treated as a no-slip wall, and all remaining outer faces of the domain are assigned symmetry conditions. Dynamic mesh is applied to the wall surrounding the beam. The fluid density is specified as $\rho = 1\ \text{kg}\cdot\text{m}^{-3}$, and the Reynolds number used in the simulation is $Re = 2 \times 10^5$. For the Fluent solver, the $k - \varepsilon$ turbulence model is adopted. The total physical simulation time is 4.4 seconds.

2.3.2. *Verification Results*

The influence of the time step is examined by varying both the structural sub-step and Fluent time step settings.

Fig. 3a shows that a large time step (0.044 s) introduces strong numerical damping, causing the oscillation to quickly settle. As the time step decreases (particularly at 0.011 s) the oscillation period aligns more closely with the finer time step cases, and the displacement response gradually becomes a clear sinusoidal pattern.

For fewer than 10 sub-steps, the displacement response exhibits artificial damping, similar to the behavior observed with coarse CFD time steps in Fig. 3b. When 20 or more sub-steps are utilized, the results converge, exhibiting a relative variation of less than 1% in the structural response.

Comparisons with the reference curve in [31] show nearly identical cycle-to-cycle amplitudes, with a frequency error of about 8.5%. Two sets of plots are generated to assess accuracy. When varying the time step, accuracy improves as the step size decreases; coarse steps (0.044 s and

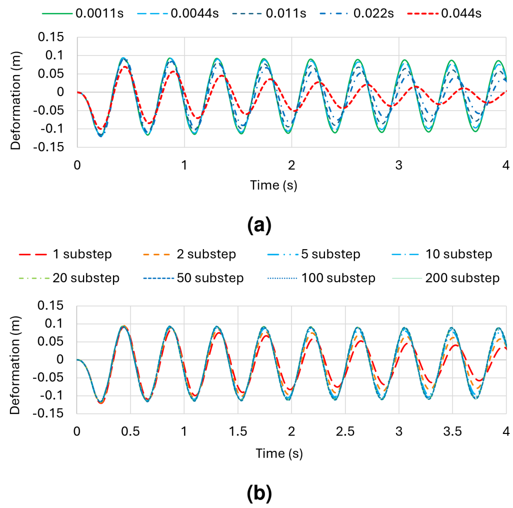

Fig. 3. a. Time-history displacement for different time step sizes. b. Time-history displacement for different sub-step settings.

0.022 s) clearly distort the oscillation period. The influence of the time step and structural sub-step settings on computation time and relative error is summarized in Table 1. Using the peak displacement of the 9th cycle (9.1 cm) as a reference, the accuracy generally improves as the step size decreases. However, refining only the CFD time step without increasing structural sub-steps can introduce artificial damping. As seen in Table 1, by fixing the time step at 0.022 s and increasing the sub-steps, the relative error drops steadily, satisfying the < 1% convergence threshold when 20 or more sub-steps are utilized.

The results indicate that an extremely fine CFD time step (0.0011 s with a single structural sub-step, resolving 400 points per cycle) yields a higher error (5.7%) and requires 16 hours of computation. This anomaly can be attributed to the accumulation of algorithmic damping. Implicit time integration schemes introduce a numerical dissipation factor at each step to suppress high-frequency noise. Consequently, excessive time step sizes accumulate this artificial energy loss, leading to amplitude decay. In contrast, the configuration utilizing 20 structural sub-steps and a 0.022 s time step requires 5 hours of computation, yielding a reduced error of 3.9%.This approach accurately resolves geometric non-linearities via Newton-Raphson iterations by dividing the aerodynamic load into smaller increments, completely avoiding the heavy penalty of compounding temporal damping. This demonstrates that excessive CFD time step refinement is computationally disproportionate; optimizing structural sub-steps yields a threefold reduction in computational time (from 16 hours to 5 hours) while

Table 1. Effect of temporal resolution on computation time and relative error.

Configuration Type	Global Time Step (s)	Structural Sub-steps	Computation Time (hours)	Relative Error (%)
Varying Global Time Step (Fixed 1 sub-step)	0.044	1	0.1	131.7
	0.022	1	0.33	65.4
	0.011	1	1.5	37.2
	0.0044	1	4	17.1
	0.0011	1	16	5.7
	0.022	1	0.33	65.4
Varying Structural Sub-Steps (Fixed 0.022 s time step)	0.022	2	0.5	37.1
	0.022	5	1.0	17.7
	0.022	10	2.5	8.4
	0.022	20	5	3.9
	0.022	50	13	3.6
	0.022	100	25	3.6
	0.022	200	50	3.6

enhancing accuracy.

Overall, dividing each oscillation period into at least 20 CFD time steps and using 20 or more structural sub-steps provides high accuracy at substantially reduced computational cost for similar FSI problems.

3. Results and discussions

3.1. Case of Cropped Delta Wing

To validate the suitability of the selected time step and sub-step strategy, a cropped delta wing model is employed as a verification case.

3.1.1. Model and Natural Frequencies

The cropped delta wing model from [32, 33] is considered in the present simulation. The wing has a leading-edge sweep angle of 47.8° and a trailing-edge sweep angle of -8.7°. The thickness (t) and half-span (b) of the model are 8.89×10^{-4} m and 0.2 m , respectively. The wing material has a density of 7833.41 kg/m^3, a Young's modulus of 206.84 GPa , and a Poisson's ratio of 0.25.

The first vibration modes of the cropped delta wing are compared with the results reported in [33], as shown in Fig. 4a.

3.1.2. Flutter Simulation of the Cropped Delta Wing

The structural model contains a total of 29,027 nodes and 5,160 elements. The wing root is fully clamped. The simulation is carried out for a physical time of 0.2 s. The fluid domain consists of a total of 1, 305, 600 hexahedral elements, as shown in the aerodynamic mesh in Fig. 4b. The time step used for the simulation is 0.0001 s, with 30 inner iterations performed for each physical time step, 20 structural sub-steps are assigned within each time step. The inlet flow conditions are specified as $M_\infty = 0.878$, Reynolds number $Re_\infty = 2.932 \times 10^6$, and free-stream dynamic pressure $q_\infty = 19.167$kPa. Turbulence is modeled using the $k-\omega$ SST turbulence model. To properly resolve the viscous sublayer and support the $k-\omega$ SST turbulence model, the near-wall mesh was heavily refined using inflation layers. The boundary layer grid was generated with a first cell height of 1×10^{-5} m and 20 prism layers, ensuring that the maximum y^+value on the wing surface was strictly maintained below 1.0. The aerodynamics of a delta wing are heavily dominated by near-wall effects, boundary layer separation, and leading-edge vortices under adverse pressure gradients. The standard $k-\varepsilon$ model was retained in the beam case exclusively to replicate the exact numerical setup of the reference study. However, this model is known to perform poorly in predicting boundary layer separation. The $k-\omega$SST formulation accurately captures these complex near-wall flow phenomena. The initial flow field is perturbed by applying a very small angle of attack of 0.1°. A comparison between the present simulation and the results reported in [33] shows that, before $t = 0.1$ s (Fig. 5), there are small discrepancies in both the oscillation period and amplitude. These differences result from using a different initialization strategy than [33], namely a small, time-decaying velocity component in the z-direction with a nominal angle of attack of 0°, such that the effective inflow velocity still corresponds to an equivalent angle of attack of 0.1°.

3.2. Case of Composite UAV Wing

Fig. 6 illustrates the structural configuration of the UAV wing, which has a wingspan of 2.9 m, a root chord length of 0.31 m, and is equipped with a winglet. The properties of Carbon Fiber (T300) are adopted from Wenzhi Wang et al. [34]. The mechanical properties of Aluminum 7075-T6 and the structural foam core (Foam M60) are obtained from standard material property databases and manufacturer

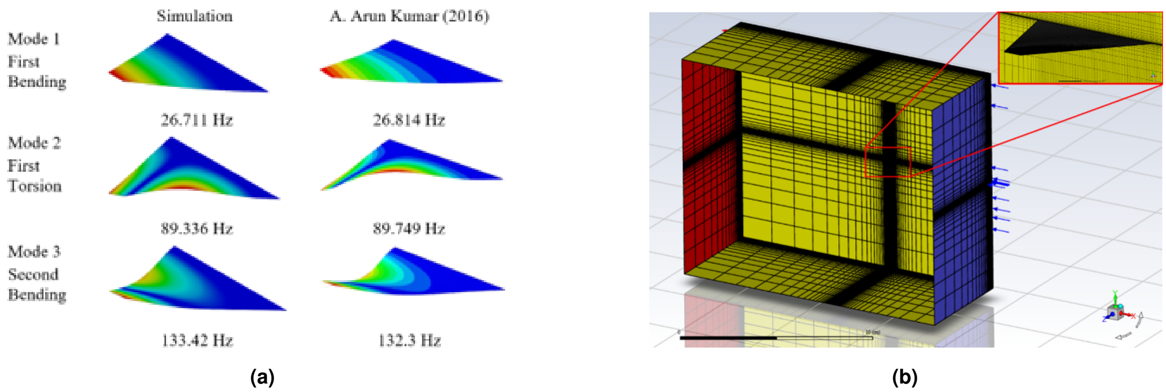

Fig. 4. a. First three natural vibration modes of the cropped delta wing. b. CFD model of the cropped delta wing

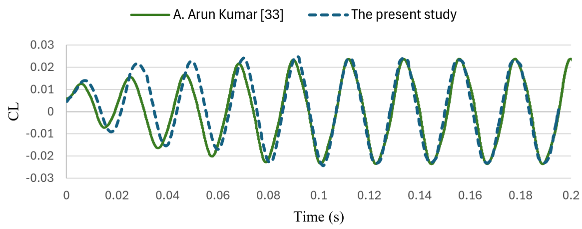

Fig. 5. Time history of C_L

technical specifications [35, 36]. Most of the wing structure is formed by interlacing multiple composite layers, with a foam core embedded inside. The detailed mechanical properties of the materials used for the UAV wing are summarized in Table 2.

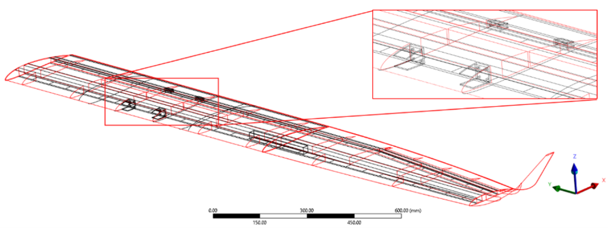

Fig. 6. Composite wing model.

3.2.1. *Static Structural Analysis*

A modal analysis is first conducted to identify the wing's fundamental vibration modes, as shown in Fig. 7. The UAV has a maximum takeoff weight (MTOW) of 26 kg and operates within a load factor range of –1 g to 3.5 g. Lift distribution is calculated using the Schrenk method (Eqs. (8) to (10)). The 3.5 g load case is evaluated to assess static structural strength, resulting in a load of 446 N on one half-wing. This distributed lift is applied to the spar in the upward direction, opposite to gravity, with the spanwise values shown in Fig. 8.

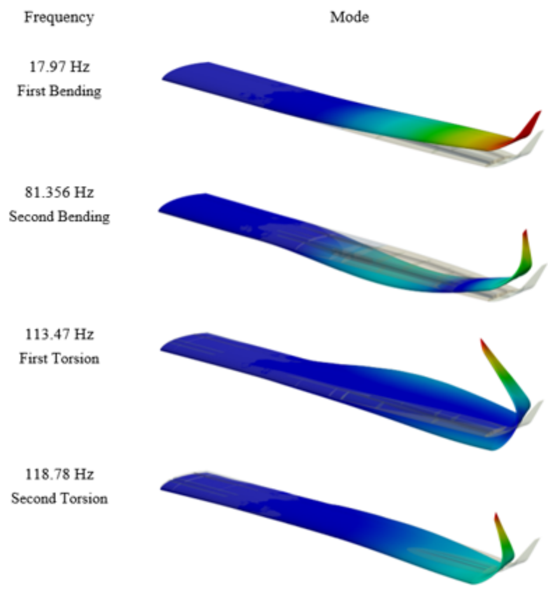

Fig. 7. First vibration modes of the wing model.

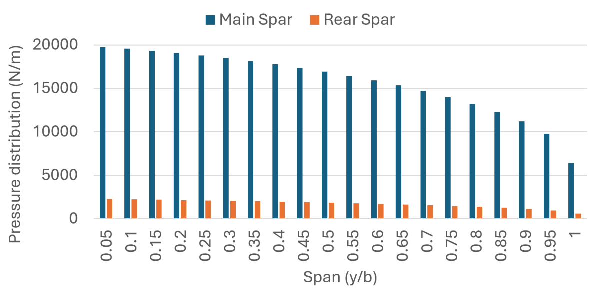

Fig. 8. 3.5g pressure distribution applied to the half-wing using the Schrenk method.

Table 2. Material properties used for the UAV wing.

Parameter	Carbon Fiber (T300)	Foam M60	Aluminum 7075-T6
Density $(\mathrm{kg/m^3})$	1484	65	2804
E1(GPa)	50.3	0.044	70
E2(GPa)	50.3	0.044	70
E3(GPa)	7.06	0.044	70
v12	0.0331	0.1	0.32
v13	0.387	0.1	0.32
v23	0.387	0.1	0.32
G12 (GPa)	2.65	0.02	26.51
G13(GPa)	2.43	0.02	26.51
G23 (GPa)	2.43	0.02	26.51
Ultimate strength (MPa)	513	0.85	560

$$L'_{\text{ellip}} = \frac{4L}{\pi b}\sqrt{1-\left(\frac{2y}{b}\right)^2} \tag{8}$$

$$L'_{\text{flat}} = \frac{2L}{(1+\lambda)b}\left(1+\frac{2y}{b}(\lambda-1)\right) \tag{9}$$

$$L'_{\text{Schrenk}} = \frac{L'_{\text{ellip}} + L'_{\text{flat}}}{2} \tag{10}$$

where: L : total lift (N) L' : lift distribution (N/m) L'_{ellip} : elliptical lift distribution (N/m) L'_{flat} : rectangular (flat-plate) lift distribution (N/m) L'_{Schrenk} : Schrenk lift distribution (N/m) λ : taper ratio b : wingspan (m) y : spanwise location (m)

According to FAR 23 standards [37], the wing deflection must not exceed 5 degrees, corresponding to a vertical displacement of no more than 12.6 cm . Under static structural analysis using the Schrenk method for load application, the wing meets all structural strength requirements, with a minimum safety factor of 1.5 and a maximum displacement of 7.93 cm, respectively.

3.2.2. *Aerodynamic Domain Analysis*

First, the lift coefficient of the wing model is computed using the aircraft's cruise speed of 100 km/h (equivalent to 27.77 m/s). The UAV operates under conditions where the dynamic viscosity is 1.5×10^{-5} kg/(m.s), the air density is 1.2 kg/m^3, and the characteristic length for the boundary layer is taken as the root chord length of 0.3 m.

For a target value of $Y^+ = 1$, the thickness of the first boundary-layer cell is determined to be 1×10^{-5} m. A total of 20 prism layers with a growth rate of 1.2 is used to ensure adequate near-wall resolution. Following the simulation, the maximum y^+value observed on the wing surface was confirmed to be 1.02 , which excellently satisfies the strict near-wall resolution requirements of the $k-\omega$ SST model. Using a half-wing area of 0.45 m^2, the computed lift coefficient is $C_L = 0.62$. The flow velocity corresponding to the 3.5 g load case is determined using Eq. (11), the corresponding flight speed required to achieve a load factor of 3.5 g is calculated to be 51.79 m/s.

$$L = \frac{1}{2}\rho \cdot V^2 \cdot S \cdot Cl \tag{11}$$

3.2.3. *One-way FSI Analysis*

A one-way FSI analysis is performed to evaluate the aerodynamic pressure distribution and structural integrity of the wing surface. Table 3 summarizes the maximum winglet displacements and minimum structural safety factors across different inflow velocities. The results indicate that at the nominal high-load velocity of 51.79 m/s, the wing maintains a robust safety factor, outperforming the predictions from the static structural analysis using the Schrenk method. However, as the flight velocity increases to 65 m/s, the intensified aerodynamic loads drive up the tip displacement and significantly reduce the safety factor, indicating that the structure is approaching its critical operational limit.

3.2.4. *Two-way FSI Analysis*

The initial bending-mode natural frequency of the structural model is 17.97 Hz, corresponding to an oscillation period of 0.0056 s. Using Eq. (7), the recommended time step is 0.0028 s. For improved resolution and higher accuracy, a slightly smaller time step of 0.0025 s is selected. The total number of time steps used in the simulation is 200, corresponding to a physical time of 0.5 seconds. The simulation cases include inlet velocities of 55.5 m/s, 65 m/s, and 75 m/s. The time-history displacement responses for these cases are shown in Fig. 9.

At the critical first bending mode natural frequency of 17.97 Hz, the total physical simulation time of 0.5 s covers approximately 9 full oscillation cycles. As illustrated in Fig. 9, the transient structural response exhibits significant positive aerodynamic damping across all evaluated velocity cases, including the extreme condition of 75 m/s. The initial perturbations decay rapidly, and the wing displacement response stabilizes into a steady state after approx-

Table 3. Structural responses from one-way FSI analysis under different inflow velocities.

Inflow Velocity (m/s)	Maximum Wing Displacement (cm) (Allowable displacement: 12.6 cm)	Minimum Safety Factor
51.79	7.59	1.72
55.50	8.68	1.50
65.00	12.33	1.06

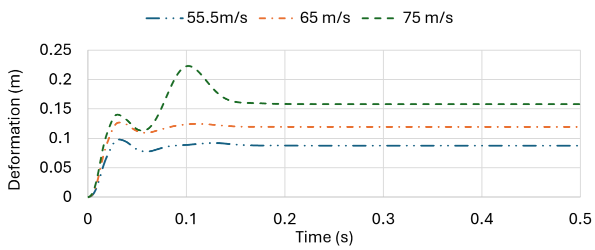

Fig. 9. Maximum wing displacement over time at different velocity: 55.5m/s; 65m/s; 75m/s.

imately 0.2 s. Because the vibration amplitude explicitly and rapidly decays rather than maintaining a neutral state or showing divergence, this duration provides a sufficient physical justification to conclude that the wing remains aeroelastically stable within the operational envelope.

The one-way FSI analysis (Section 3.2.3) is limited to evaluating the static aeroelastic deformation and structural strength under peak aerodynamic loads, indicating a critical structural yield limit near 65 m/s. However, one-way coupling cannot predict dynamic instabilities. In contrast, the two-way FSI analysis accurately captures the dynamic energy exchange between the fluid and the structure. It reveals that the fluid acts as a positive aerodynamic damper rather than an exciter.

However, it is important to acknowledge the limitations associated with this simulation duration. While 0.5 s simulation is adequate to demonstrate the initial suppression of flutter through positive aerodynamic damping, it may not capture long-term aeroelastic phenomena, such as low-frequency limit-cycle oscillations (LCOs) or gradual flow-induced fatigue effects that could develop over extended periods. Extending the physical simulation time would provide a more comprehensive understanding of these long-term behaviors; however, doing so is currently restricted by the substantial computational cost inherent to high-fidelity bidirectional FSI simulations.

4. Conclusions

This study analyzed how time step size and structural sub-step affect FSI simulation accuracy. Results show that using about 20 points per oscillation cycle is sufficient for capturing the dynamics, and more than 20 structural sub-steps per time step offers the best balance between accuracy and computational cost. Applying these settings to the cropped delta wing yields results consistent with the reference study, confirming the reliability of the proposed approach. For the realistic composite wing, no flutter occurs within the UAV's operating velocity range; structural failure would occur first at the limit condition. Even at 75 m/s, the wing remains self-stabilizing. At 51.79 m/s and 55.5 m/s, both displacement and safety factor remain acceptable.

While the simulations have been validated through benchmark cases, experimental testing is still needed for maximum confidence. Nevertheless, two-way FSI remains an effective and cost-efficient alternative to extensive physical experiments for similar or more complex configurations. This work successfully performed FSI analysis on a composite fixed-wing structure. Future studies may refine the design by adjusting wing geometry or span to assess flutter in larger UAVs, such as MALE platforms, or extend the investigation to flutter behavior in composite helicopter rotor blades and other rotary-wing systems.

Acknowledgements

This research is funded by the Viettel High Technology Industries Corporation in collaboration with Hanoi University of Science and Technology. The authors gratefully acknowledge the support and cooperation provided throughout the execution of this study.

References

[1] B. Wang, L. Feng, L. Xu, H. Gao, X. Luo, and N. Qi, (2025) *"Three-dimensional fluid–structure interaction modelling of the venous valve using immersed boundary/finite element method"* **Computers in Biology and Medicine *185***: 109450. DOI: 10.1016/j.compbiomed.2024.109450.

[2] F. Marcinnò, C. Vergara, L. Giovannacci, A. Quarteroni, and G. Prouse, (2024) *"Computational fluid-structure interaction analysis of the end-to-side radio-cephalic arteriovenous fistula"* **Computer Methods and Programs in Biomedicine *249***: 108146. DOI: 10.1016/j.cmpb.2024.108146.

[3] A. M. Tango, A. Monteleone, A. Ducci, and G. Burriesci, (2025) *"Analysis of the haemodynamic changes caused by surgical and transcatheter aortic valve replacements by means fluid-structure interaction simulations"* **Computers in Biology and Medicine *186***: 109673. DOI: 10.1016/j.compbiomed.2025.109673.

[4] L. Feng, H. Gao, and X. Luo, (2024) *"Whole-heart modelling with valves in a fluid–structure interaction framework"* **Computer Methods in Applied Mechanics and Engineering *420***: 116724. DOI: 10.1016/j.cma.2023.116724.

[5] S. Qashqaie Abdi and K. Hassani, (2023) *"The study of the relationship between unicuspid aortic valve insufficiency and heart disease by fluid-structure interaction modeling"* **Biomedical Engineering Advances *5***: 100079. DOI: 10.1016/j.bea.2023.100079.

[6] L. Cai, T. Zhao, Y. Wang, X. Luo, and H. Gao, (2023) *"Fluid–structure interaction simulation of pathological mitral valve dynamics in a coupled mitral valve-left ventricle model"* **Intelligent Medicine *3***(2): 104–114. DOI: 10.1016/j.imed.2022.06.005.

[7] A. Souche and K. Valen-Sendstad, (2022) *"High-fidelity fluid structure interaction simulations of turbulent-like aneurysm flows reveals high-frequency narrowband wall vibrations: A stimulus of mechanobiological relevance?"* **Journal of Biomechanics *145***: 111369. DOI: 10.1016/j.jbiomech.2022.111369.

[8] Y. Mai, S. Wen, J. Zhang, Y. Lan, and G. Huang, (2025) *"Analysis of the two-way fluid-structure interaction between the rice canopy and the downwash airflow of a quadcopter UAV"* **Biosystems Engineering *250***: 343–364. DOI: 10.1016/j.biosystemseng.2025.01.005.

[9] H. Cui, C. Wang, X. Liu, X. Liu, J. Yuan, and Y. Liu, (2023) *"Prediction of the distribution of airflow within the cotton canopy using fluid–structure interaction simulation and machine-learning methods"* **Biosystems Engineering *232***: 51–66. DOI: 10.1016/j.biosystemseng.2023.06.011.

[10] X. Liao, C. G. Koh, and Y. K. Chow, (2025) *"A hybrid strategy for numerical simulations of fluid-structure interaction problems in ocean engineering"* **Applied Ocean Research *155***: 104433. DOI: 10.1016/j.apor.2025.104433.

[11] I. Prüter, F. Spröer, K. Keimer, O. Lojek, C. Windt, D. Schürenkamp, H. Bihs, I. Nistor, and N. Goseberg, (2025) *"A comprehensive numerical study on the current-induced fluid–structure interaction of flexible submerged vegetation"* **Journal of Fluids and Structures *133***: 104232. DOI: 10.1016/j.jfluidstructs.2024.104232.

[12] H. K. Sakran, M. S. A. Aziz, and C. Y. Khor, (2024) *"Blade Wrap Angle Impact on Centrifugal Pump Performance: Entropy Generation and Fluid-Structure Interaction Analysis"* **Computer Modeling in Engineering & Sciences *140***(1): 109–137. DOI: 10.32604/cmes.2024.047245.

[13] N. B. Darbhamulla and R. K. Jaiman, (2024) *"A finite element framework for fluid–structure interaction of turbulent cavitating flows with flexible structures"* **Computers & Fluids *277***: 106283. DOI: 10.1016/j.compfluid.2024.106283.

[14] M. R. Firdaus, M. R. Mahalik, A. Jusuf, S. Wicaksono, L. Gunawan, and T. Dirgantara, (2024) *"Modelling Strategies to Simulate the Fluid-Structure Interaction of Amphibious Aircraft Float Structure"* **Procedia Structural Integrity *52***: 309–322. DOI: 10.1016/j.prostr.2023.12.031.

[15] P. Shakya, M. Thomas, A. C. Seibi, M. Shekaramiz, and M. A. S. Masoum, (2024) *"Fluid-structure interaction and life prediction of small-scale damaged horizontal axis wind turbine blades"* **Results in Engineering *23***: 102388. DOI: 10.1016/j.rineng.2024.102388.

[16] L. Yuan, Z. Liu, L. Li, and M. Lin, (2023) *"Analysis of the Influence of the Blade Deformation on Wind Turbine Output Power in the Framework of a Bidirectional Fluid-Structure Interaction Model"* **Fluid Dynamics & Materials Processing *19***(5): 1129–1141. DOI: 10.32604/fdmp.2023.023538.

[17] Y. Cui, L. Wang, J. Ru, and J. Wu, (2023) *"Analysis and Optimization of Flow-Guided Structure Based on Fluid-Structure Interaction"* **Fluid Dynamics & Materials Processing *19***(6): 1573–1584. DOI: 10.32604/fdmp.2023.024873.

[18] M. Mihaila-Andres, C. Rotaru, and P. G. Matei, (2015) *"Staggered Approach for Fluid-Structure Interaction Phenomena of an AGARD 445.6 Wing Using Commercial CFD/CSM Software"* **Journal of Aerospace Engineering *28***(4): DOI: 10.1061/(asce)as.1943-5525.0000427.

[19] N. Di Domenico, C. Groth, A. Wade, T. Berg, and M. E. Biancolini, (2018) *"Fluid structure interaction analysis: vortex shedding induced vibrations"* **Procedia Structural Integrity *8***: 422–432. DOI: 10.1016/j.prostr.2017.12.042.

[20] A. J. Torregrosa, A. Gil, P. Quintero, and A. Cremades, (2022) *"On the effects of orthotropic materials in flutter protection of wind turbine flexible blades"* **Journal of Wind Engineering and Industrial Aerodynamics** ***227***: 105055. DOI: 10.1016/j.jweia.2022.105055.

[21] F. Salmon and L. Chatellier, (2022) *"3D fluid–structure interaction simulation of an hydrofoil at low Reynolds number"* **Journal of Fluids and Structures** ***111***: 103573. DOI: 10.1016/j.jfluidstructs.2022.103573.

[22] W. Guo, Y. Shui, L. Nie, and G. Chen, (2024) *"Fluid-structure interaction simulation for multi-body flexible morphing structures"* **Chinese Journal of Aeronautics** ***37***(2): 137–147. DOI: 10.1016/j.cja.2023.09.009.

[23] J. Pflüger and C. Breitsamter, (2024) *"Gust response of an elasto-flexible morphing wing using fluid–structure interaction simulations"* **Chinese Journal of Aeronautics** ***37***(2): 45–57. DOI: 10.1016/j.cja.2023.12.017.

[24] Y. Guo, W. Yang, Y. Dong, and D. Xue, (2024) *"Resonance mechanism of flapping wing based on fluid structure interaction simulation"* **Chinese Journal of Aeronautics** ***37***(5): 243–262. DOI: 10.1016/j.cja.2024.01.011.

[25] Y. Dai, Y. Hu, Y. Wu, C. Song, and C. Yang, (2025) *"Effect of leading-edge and trailing-edge camber morphing on gust load for an elastic wing"* **Chinese Journal of Aeronautics** ***38***(4): 103245. DOI: 10.1016/j.cja.2024.09.021.

[26] T. Schwentner and T.-P. Fries, (2024) *"Fully Coupled, Higher-Order, Block-Structured Mesh Generation in Fluid–Structure Interaction"* **International Journal for Numerical Methods in Fluids** ***97***(3): 359–377. DOI: 10.1002/fld.5355.

[27] M. R. Rajanna, E. L. Johnson, N. Liu, A. Korobenko, Y. Bazilevs, and M.-C. Hsu, (2022) *"Fluid–structure interaction modeling with nonmatching interface discretizations for compressible flow problems: Computational framework and validation study"* **Mathematical Models and Methods in Applied Sciences** ***32***(12): 2497–2528. DOI: 10.1142/s0218202522500592.

[28] B. Li, W. Sun, Y. Xie, and W. Yu, (2024) *"Optimal L2 Error Analysis of a Loosely Coupled Finite Element Scheme for Thin-Structure Interactions"* **SIAM Journal on Numerical Analysis** ***62***(4): 1782–1813. DOI: 10.1137/23m1578401.

[29] M. Bukač, G. Fu, A. Seboldt, and C. Trenchea, (2023) *"Time-adaptive partitioned method for fluid-structure interaction problems with thick structures"* **Journal of Computational Physics** ***473***: 111708. DOI: 10.1016/j.jcp.2022.111708.

[30] J. Čečrdle. *Whirl Flutter of Turboprop Aircraft Structures*. Elsevier, 2015. DOI: 10.1016/C2014-0-01800-X.

[31] A. K. Slone, K. Pericleous, C. Bailey, and M. Cross, (2002) *"Dynamic fluid–structure interaction using finite volume unstructured mesh procedures"* **Computers & Structures** ***80***(5–6): 371–390. DOI: 10.1016/s0045-7949(01)00177-8.

[32] C. Peng and J. Han, (2011) *"Numerical investigation of the effects of structural geometric and material nonlinearities on limit-cycle oscillation of a cropped delta wing"* **Journal of Fluids and Structures** ***27***(4): 611–622. DOI: 10.1016/j.jfluidstructs.2011.03.015.

[33] A. A. Kumar, N. Manoj, A. K. Onkar, and M. Manjuprasad, (2016) *"Fluid-Structure Interaction Analysis of a Cropped Delta Wing"* **Procedia Engineering** ***144***: 1205–1212. DOI: 10.1016/j.proeng.2016.05.102.

[34] W. Wang, Y. Dai, C. Zhang, X. Gao, and M. Zhao, (2016) *"Micromechanical Modeling of Fiber-Reinforced Composites with Statistically Equivalent Random Fiber Distribution"* **Materials** ***9***(8): 624. DOI: 10.3390/ma9080624.

[35] MakeItFrom.com. *7075-T6 Aluminum Material Properties Database*.

[36] Corecell™ M-foam structural core data sheet. *Gurit*. 2021.

[37] Federal Aviation Administration. *Airworthiness Standard FAR Part 23, Part 25*. 2024.